scientific reports

Check for updates

OPEN

Solar-matched S-scheme ZnO/g-C_3N_4 for visible light-driven paracetamol degradation

Fahad Hassan[1]✉, Sumina Namboorimadathil Backer[1], Ismail W. Almanassra[1], Muataz Ali Atieh[1,2], Mady Elbahri[3]✉ & Abdallah Shanableh[1,4]✉

In pursuit of an efficient visible light driven photocatalyst for paracetamol degradation in wastewater, we have fabricated the ZnO/g-C_3N_4 S-Scheme photocatalysts and explored the optimal percentage to form a composite of graphitic carbon nitride (g-C_3N_4) with zinc oxide (ZnO) for enhanced performance. Our study aimed to address the urgent need for a catalyst capable of environmentally friendly degradation of paracetamol, a common pharmaceutical pollutant, using visible light conditions. Here, we tailored the band gap of a photocatalyst to match solar radiation as a transformative advancement in environmental catalysis. Notably, the optimized composite, containing 10 wt.% g-C_3N_4 with ZnO, demonstrated outstanding paracetamol degradation efficiency of 95% within a mere 60-min exposure to visible light. This marked enhancement represented a 2.24-fold increase in the reaction rate compared to lower wt. percentage composites (3 wt.% g-C_3N_4) and pristine g-C_3N_4. The exceptional photocatalytic activity of the optimized composite can be attributed to the band gap narrowing that closely matched the maximum solar radiation spectrum. This, coupled with efficient charge transfer mechanisms through S-scheme heterojunction formation and an abundance of active sites due to increased surface area and reduced particle size, contributed to the remarkable performance. Trapping experiments identified hydroxyl radicals as the primary reactive species responsible for paracetamol photoreduction. Furthermore, the synthesized ZnO/g-C_3N_4 composite exhibited exceptional photostability and reusability, underscoring its practical applicability. Thus, this research marks a significant stride towards the development of an effective and sustainable visible light photocatalyst for the removal of pharmaceutical contaminants from aquatic environments.

Keywords Zinc oxide, Graphitic carbon nitride, Photodegradation, Band alignment, Degradation pathway

In recent years, pharmaceutical compounds present in wastewater have evolved paramount environmental concerns affecting aquatic and human life[1]. A plethora of drugs including antiseptics, antibiotics, disinfectants, and anti-inflammatory contents are being used extensively[2]. Above all, one of the most heavily consumed drugs is paracetamol, a well-known antipyretic and analgesic[3]. In connection to the enormous production and usage, paracetamol has been found commonly in environment, specifically in wastewater with 0.01–0.03 mg/L, which advocates the status of an unsafe drug[3]. The catastrophic effects of the contaminant could range from failure of many organs to unexpected death of humans and animals[3]. To eradicate the mentioned above, it is required to reduce the paracetamol into nontoxic products by an effective method. Many advanced processes of oxidation such as ultraviolet (UV) oxidation, ozonation[4], electrochemical[5] and heterogeneous photocatalysis[6] have been utilized to curb the unwanted pharmaceutical compounds. Several metal oxide semiconductors having a higher band gap are formulated[7] which includes titanium oxide (TiO_2), ZnO and graphene-oriented metal oxides, these materials could disintegrate the organic pollutants by catalysis in UV light irradiation[8–10]. Moreover, a huge number of 2D S-scheme heterojunction photocatalyst systems have also been used for photocatalysis with various configurations of dimensions[11,12].

Due to the immaculate mineralization activity for aqueous contaminants, destruction of organic-molecules, specific-organisms, and toxic metal ions, ZnO has been the most promising material[13,14] which has executed its

[1]Research Institute of Sciences and Engineering, University of Sharjah, Sharjah 27272, UAE. [2]Chemical and Water Desalination Engineering Program, College of Engineering, University of Sharjah, Sharjah 27272, UAE. [3]Nanochemistry and Nanoengineering, Department of Chemistry and Materials Science, School of Chemical Engineering, Aalto University, 02150 Espoo, Finland. [4]Department of Civil and Environmental Engineering, College of Engineering, University of Sharjah, Sharjah 27272, UAE. ✉email: fahad.hassan@sharjah.ac.ae; mady.elbahri@aalto.fi; shanableh@sharjah.ac.ae

application in biomedical and environmental research. Although the unmatched redox potential and electron mobility has second the extensive use of ZnO as photocatalyst[15–17], the low absorption in visible light, low photo absorption sensitivity and weak charge carrier separation have obstructed its practical applications. Therefore, the researchers have put their efforts to modify the stability and performance of ZnO photocatalyst by heteroatom-doping[18,19], novel-metal composite[20,21], surface functionalization with polymers such as polydopamine[22] or coupling it with a semiconductor[10,23–25]. Furthermore, the fabrication of ZnO based S-scheme heterojunctions has evolved as an advanced solution to overcome the limitations attributed to the use of pristine ZnO in photocatalysis[12,26–28]. Gaowei Han et al., performed a study on inverse Opal ZnO@Polydopamine S-Scheme heterojunctions for H_2O_2 production, the unique formation of S-scheme impacted effective separation/transport of charge carriers, which resulted in the enhancement of overall photocatalytic properties of ZnO[22]. The formation of ZnO based S-scheme heterojunction is more feasible approach considering the superior performances in various photocatalytic reactions, it majorly utilized the synergistic effect of internal electric field and band bending, detailed study has been done on this advancement detailing the improvements in the photocatalysis[26]. Synergistic effect of IIEF and band bending in S-scheme heterojunctions overcomes the drawbacks of PC migration in TZS and ASSZH. Therefore, the S-scheme heterojunction achieves spatial separation of powerful PC, resulting in enhanced photocatalytic performance. Construction of ZnO-based S-scheme heterojunction provides a feasible approach to achieve efficient photocatalytic pollutant degradation.

Meanwhile, g-C_3N_4, a semiconductor having many advantages such as easy preparation from low cost and widely available precursors, narrow band gap, having no harmful metals, baring excellent thermal and chemical stability[29,30], has been used by scientists for several applications[31,32] which include, biosensors[33], biochemical[34] and photo/electrochemical applications[35]. An effective and novel way to modify the light absorbance with increased charge separation is by forming a nanocomposite by coupling ZnO and g-C_3N_4[36]. Ball milling and two step chemisorption method has been adopted in earlier studies[37,38] to fabricate ZnO/g-C_3N_4 composite. Formation of g-C_3N_4 decorated ZnO composites were reported by Zhu et al.[39] by calcination method. Further, vapor condensation was also used to coat the ZnO nanorods with g-C_3N_4[40]. For the optimum photocatalytic activity, the synthesis method plays a vital role in establishing a junction between g-C_3N_4 and ZnO[39]. Recently, flower like structure of g-C_3N_4 and $ZnIn_2S_4$ was reported which was functionalized by benzoic for hydrogen evolution with photocatalysis and to degrade the tetracycline hydrochloride, they used novel BiOCII/β-Bi_2O_3 composite under sunlight simulator[41]. Moreover, functional g-C_3N_4 has been formulated with a new design by co-polymerization[42]. Furthermore, noticeable progress in ZnO and g-C_3N_4 based S-scheme photocatalyst has been seen due to their unmatched electronic structure and stability. An enhancement of photocatalytic performance has been observed in S-scheme photocatalyst due to efficient charge transfer and separation which is highlighted in the recent studies in terms of pollutant degradation, CO_2 reduction and water splitting[43].

The significant efforts directed towards enhancing the efficiency of photocatalysts for visible light-driven processes of such composite, the utilization of g-C_3N_4 as a seed at very low concentrations, coupled with solid-state transformation techniques to tailor the morphology, surface porosity, and concentration while simultaneously engineering the band gap of ZnO to match the maximum solar absorption, represents an underexplored frontier in this domain. However, tailoring the band gap of a photocatalyst to match the solar radiation spectrum represents a pivotal advancement in the field of photocatalysis[26] with profound implications for the degradation of contaminants.

Considering the above-mentioned traits we have fabricated a ZnO/g-C_3N_4 S-scheme photocatalyst and to the best of our knowledge, there has been a conspicuous absence of research addressing the crucial aspects mentioned above. Furthermore, the integration of such a structure for visible light-assisted catalysis of paracetamol, using a ZnO/g-C_3N_4 S-scheme photocatalytic composite, remains uncharted territory in the existing literature. Considering this, our study breaks new ground by introducing a novel approach. We present a meticulous synthesis of a composite material containing g-C_3N_4 and ZnO, achieved through a combination of hydrothermal and thermal oxidative methods with varying g-C_3N_4 ratios.

Our comprehensive investigation includes a thorough characterization of the synthesized composite, involving X-ray diffraction (XRD), Fourier transform infrared (FTIR) spectroscopy, field emission scanning electron microscopy (FESEM), energy dispersive X-ray spectroscopy (EDS), UV–Vis spectroscopy, Brunauer, Emmett, and Teller (BET) analysis, X-ray photoelectron spectroscopy (XPS), and liquid chromatography quadrupole time-of-flight mass spectrometry (LC-QTOF-MS). Through this analysis, we have systematically explored the structural, textural, and optical properties of our material.

The results of our study reveal the remarkable efficiency of this composite in the degradation of paracetamol in water under visible light irradiation. This enhanced performance can be attributed to several factors, including a reduction in the band gap, an increase in the specific surface area (S_{BET}), and the effective transfer of charge carriers within the prepared photocatalytic composite. Notably, we have determined that a specific concentration of g-C_3N_4 in ZnO plays a pivotal role in the mineralization process. Additionally, we delve into the mechanism of band alignment through ultraviolet photoelectron spectroscopy (UPS) to provide insights into the charge transfer processes within the composite. This research represents a significant step forward in the quest for advanced photocatalysts tailored for visible light-driven applications, offering both a thorough characterization and mechanistic exploration of the synthesized composite material.

Experimental

Chemicals and reagents

Zinc chloride pure ≥ 99.9%, was obtained from Sisco Research laboratories, India. Melamine ($C_3H_6N_6$, ≥ 99%) was bought from Sigma Aldrich, Germany. Sodium hydroxide (NaOH, 98%) pellets, and Methanol (CH_3OH) were obtained from SD Fine-chem Limited, India. Paracetamol ($C_8H_9NO_2$, Hema Pharmaceuticals, India, 99.98%)

was selected as main pollutant for this study. As supplied, all analytical grade chemicals were utilized without performing any further treatments. Deionized (DI) water (0.055 μS cm^{1}) was obtained using NANOpure Diamond by Barnstead, USA and was utilized throughout in the study.

Synthesis of catalysts

Synthesis of g-C_3N_4 Melamine was utilized to synthesize g-C_3N_4 as reported earlier[44]. Briefly, melamine (15 g) contained in a semi closed ceramic-crucible was heated in the tube furnace at a temperature of 550 °C with heating rate of 2 °C/min for 4 h. The sample obtained by the reaction was let cool to 22 °C naturally and eventually the yellow g-C_3N_4 powder was collected. Which was further washed with DI water and then dried at 60 °C for 12 h and eventually grounded in mortar to obtain fine powder for composite preparation.

Synthesis of ZnO For ZnO preparation, firstly, a homogeneous solution $ZnCl_2$ was prepared by solubilizing 13.6 g $ZnCl_2$ in DI water (100 mL), labeled as solution A. Secondly, solution B was prepared by adding 3.9 g of NaOH in 50 mL of DI water at normal temperature. Later, solution A was heated to 35 °C with constant vigorous stirring while solution B was added to it in dropwise, precipitates of $Zn(OH)_2$ were formed at this stage. The mixture was kept on stirring under same conditions for an hour to dissolve the precipitate completely and to get a homogeneous solution. The obtained homogeneous solution was then added to teflon lined reactor assembly for hydrothermal treatment at 120 °C for 24 h. After the treatment, the sample contained into a petri dish was left in the oven for drying at 60 °C for 12 h. The product was finally grounded in mortar to collect the fine powder of ZnO.

Synthesis of ZnO/g-C_3N_4 composite To obtain a variety of g-C_3N_4 concentrations in composites, 0.03, 0.05, 0.1 and 0.2 g of already prepared g-C_3N_4 was added separately to 20 mL of methanol with 1 g of ZnO each to get ZnO/g-C_3N_4 composites of wt.% 3, 5,10 and 20 wt.%. The solution was kept at a constant stirring and heating at 50 °C till evaporation of methanol. The obtained product was then shifted to semi closed ceramic crucibles to heat at 500 °C for 2 h and 5 °C/min heating rate. The obtained composites were grounded in the mortar to obtain fine powder.

Preparation of paracetamol stock A 30 mg/L solution of paracetamol drug was prepared as initial concentration for the photodegradation analysis. An amount of 0.03 g paracetamol weighed accurately and added into 1000 mL of DI water with constant stirring for an hour to completely dissolve and form a homogenous stock solution.

Characterizations

Powder XRD was performed using Bruker D8 advance and the diffraction patterns were collected between 10 and 80° of 2θ. XPS and UV-UPS was performed using XPS Nexsa G2, Thermo scientific, U.K with monochromatized Al- Kα radiation (1486.6 eV) under ultra-high vacuum (~10 − 9 mbar), data was interpreted using the software Avantage V6.4.1. FTIR data was collected using Jasco 6300, the spectra were obtained in the range of wavenumber 500 – 4000 cm^{-1}. FESEM was done for surface morphology, Tescan Vega 3XMU was utilized for the images and EDS. Specific surface area (S_{BET}) was obtained using, NOVA tech Lx^2 NT2LX-1, adsorption isotherm was analyzed on standard BET pressure range $0.05 < P/P_o < 0.3$, employing nitrogen adsorbate with molecular area 16.2 $Å^2$ at 77 K. UV–VIS absorbance spectra were investigated with Shimadzu UV-2600i, while the diffusive reflectance spectra were obtained by an integrated sphere attachment to the device.

Photocatalytic Study

Photocatalytic performances studies of the fabricated catalysts were conducted under Xenon light source of 500 W power fitted with 420 nm UV cutoff filter. Briefly, the desired amount of the catalyst was added to a beaker containing 100 mL of paracetamol solution and placed at a distance of 5 cm under the light source. Initially, the solution was agitated in dark for 30 min to achieve adsorption desorption equilibrium. Later, visible light irradiation was employed on the solution for 60 min to initiate the photocatalytic process. At time intervals, 3 mL aliquots were taken for analysis by filtering through a 0.45 μm syringe-filter. The concentration of paracetamol was measured spectrophotometrically by absorbance in the solution at a wavelength of $\lambda_{max} = 245$ nm. Equation (1) was used to determine the percentage photodegradation of paracetamol, while the kinetic behavior of photodegradation was analyzed by fitting the investigated data with first-order kinetic model using Eq. (2).

$$Degradation(\%) = \frac{C_0 - C_t}{C_0} \times 100\% \tag{1}$$

$$\ln\left(\frac{C_t}{C_0}\right) = -kt \tag{2}$$

Here, C_0 (mg/L) is absorbance of the solution after the adsorption process at 30 min in dark and C_t (mg/L) is the absorbance of the pharmaceutical solution at time t, k is the first-order rate constant.

The principal charge carriers accountable for degradation were elucidated by undertaking scavenging/trapping experiments. In our experiments, isopropanol (IPA, 10 mM), ammonium oxalate (AO, 10 mM) and p-benzoquinone (BQ, 10 mM) were added separately to the photocatalytic reaction conditions, these chemicals acted as scavengers for hydroxyl radical, hole and superoxide radical, respectively. For the reusability experiment, the solution was centrifuged after photocatalysis at 5000 rpm for five minutes, solid particles obtained by centrifugation were used again under same conditions for degradation. The pH of solution was altered between 4 and 11 to analyze the influence of pH on the photocatalytic effectiveness. The concentration of paracetamol was varied between 10 and 80 mg/L to identify the optimized value. Moreover, the amount of photocatalyst in degradation experiments was also changed between 10 and 25 mg with an increment of 5 mg in each experiment.

Results and discussion

Materials characterization

The pure ZnO diffraction peaks as illustrated in Fig. 1a at 2θ of 31.7°, 34.5°, 36.3°, 47.6°, 56.7°, 62.8° and 68.1° correspond to (100), (002), (101), (102), (110), (103) and (200) planes respectively (JCPDS: 36-1451) validated the formation of wurtzite phase of ZnO[45]. For pristine g-C_3N_4, well-defined peaks at 12.8° and 27.3° were observed, which were referred to the diffraction planes (100) and (002) respectively (ICDD 00-050-1250)[46]. These peaks correspond to the interlayer and interplanar stacking of graphitic materials[47]. The smaller peaks at 12.8° corresponding (100) could be referred to in-plane structural arrangement of g-C_3N_4, for instance, h^+ to h^+ distance of nitride-pores[48]. Moreover, the diffraction patterns of all ZnO/g-C_3N_4 composites portray peaks matching ZnO along with a small peak at 27.3° corresponding to g-C_3N_4 suggesting the successful creation of composite between g-C_3N_4 and ZnO[49]. Furthermore, peak intensity ratio of g-C_3N_4 (002) to ZnO (101) is calculated for each composite, depicted in Table 1. For the ZnO/g-C_3N_4 composites (3, 5,10 and 20 wt.%), ratio was found to be increased which anticipated to the increased amount of g-C_3N_4.

The XPS was performed to analyze the surface elemental composition of the composites. XPS survey scan presented in Fig. 1b confirms the presence of Zn, O, C and N elements, indicating the successful formation of composite between g-C_3N_4 and ZnO, where the pristine g-C_3N_4 only showed the presence of C and N elements as expected. Atomic percentage (At%) calculation of synthesized material was estimated from XPS survey spectra which is tabulated in Table 1. The increased At% of C and N in the composite was attributed to the increased loading of g-C_3N_4. For instance, it is clearly evident from the Table 1 that the atomic percentage of N in the composites was increased to 1.37, 2.24, 2.81 and 7.78 At% for ZnO/g-$C_3N_4$3%, ZnO/g-$C_3N_4$5%, ZnO/g-$C_3N_4$10% and ZnO/g-$C_3N_4$20%, respectively, ensuring the composition of g-C_3N_4 in the composites.

The structural information of the synthesized material in terms of functional groups was studied by FTIR and the outcomes are illustrated in Fig. 1c. The two peaks visible at wavenumber 1232 cm^{-1} and 1640, demonstrated in g-C_3N_4 spectrum, were attributed respectively to C–N and C=N stretching[50]. The evident peak corresponding to 810 cm^{-1} could be anticipated for the s-trizine ring breathing modes[51]. The broad absorption band in ZnO spectrum around 3000–3400 cm^{-1} was referred as the stretching vibration in $-NH_2$ by N–H bonds and/or = N–H amines in addition to the hydroxyl groups which contains water molecules that are chemically and/or physically adsorbed[50,52]. The presence of main g-C_3N_4 characteristic peaks in ZnO/g-C_3N_4 suggested the appearance of structural features of g-C_3N_4 in the composite. Moreover, the increasing absorbance intensity was observed at 1232–1640 cm^{-1} as the amount of g-C_3N_4 increased[52]. Therefore, the FTIR analysis confirmed the occurrence of fundamental characteristic peaks pertaining to pure ZnO and pristine g-C_3N_4 in the composites.

Surface morphology of unblended ZnO, pristine g-C_3N_4 and their composites was investigated by FESEM. Figure 2a–f represented the large-scale morphology of synthesized materials. The high magnification FESEM image of ZnO (Fig. 2a') possessed rod-like morphology[53] having an average length of 2.77 µm, it has regular and almost uniform surface structure evidently demonstrated polyhexagonal crystal corresponds to the wurtzite phase of ZnO[45]. Figure 2b' shows that g-C_3N_4 existed in thick dense aggregates with a mean size of 2.82 µm and a morphology resembling layered sheet as expected for graphitic materials[54]. The FESEM images (Fig. 2c'–f')

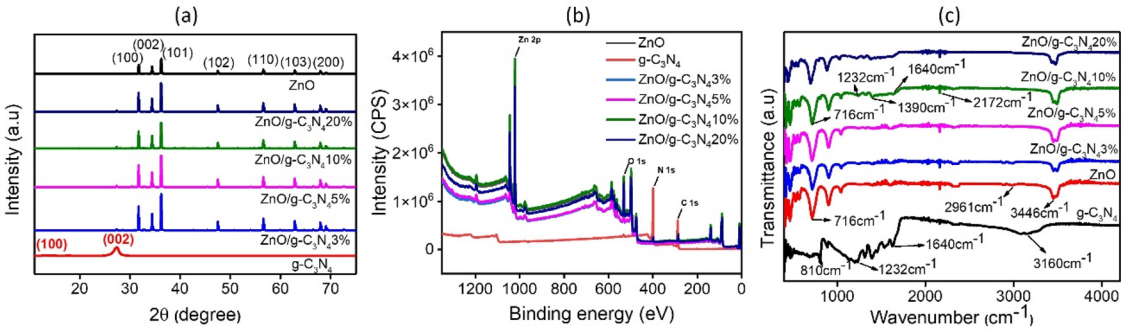

Figure 1. (**a**) XRD patterns of g-C_3N_4, ZnO and ZnO/g-C_3N_4 composites (**b**) survey scan of g-C_3N_4, ZnO and ZnO/g-C_3N_4 composites (**c**) FTIR spectra of g-C_3N_4, ZnO and ZnO/g-C_3N_4 composites.

	ZnO	g-C_3N_4	ZnO/g-C_3N_4 3%	ZnO/g-C_3N_4 5%	ZnO/g-C_3N_4 10%	ZnO/gC_3N_4 20%
At%: Zn	35.51	–	39.99	40.22	38.86	34.61
At%: O	45.19	1.85	40.48	38.38	40.35	37.35
At%: C	–	42.43	15.64	16.83	17.97	20.26
At%: N	–	55.72	1.37	2.24	2.81	7.78
$I_{(002)}/I_{(101)}$	–	–	0.023	0.038	0.047	0.063

Table 1. XPS surface elemental composition of synthesized material and XRD peak intensity ratio of g-C_3N_4 (002) to ZnO (101).

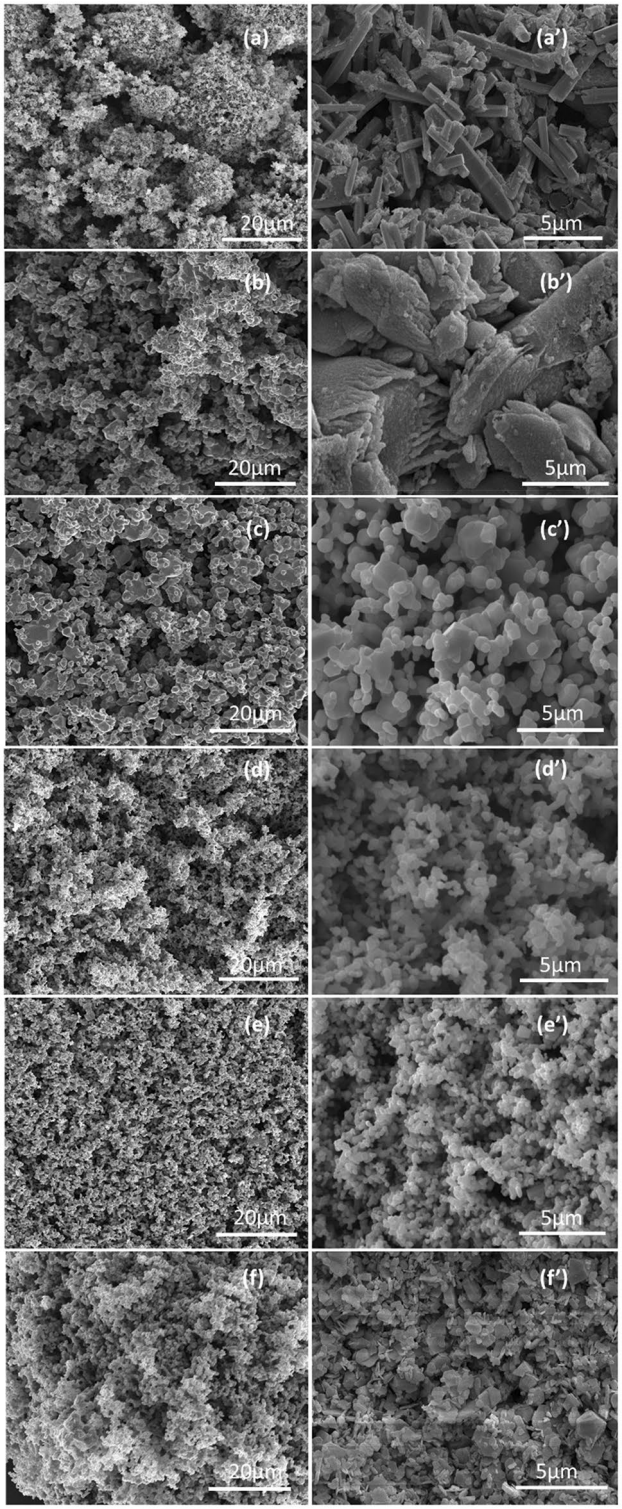

Figure 2. FESEM low and high magnification images of (**a**,**a'**) ZnO, (**b**,**b'**) g-C_3N_4, (**c**,**c'**) ZnO/g-$C_3N_4$3%, (**d**,**d'**) ZnO/g-$C_3N_4$5% (**e**,**e'**) ZnO/g-$C_3N_4$10% (**f**,**f'**) ZnO/g-$C_3N_4$20%.

revealed that morphologies of ZnO/g-C_3N_4 composites are evidently unlike that of ZnO and g-C_3N_4 alone. As the mass loading of the g-C_3N_4 increased from 3 to 20 wt.%, coral like morphology was found to be formed[55] which was different from the parent elements hence confirming the formation of composite as observed in the earlier studies[56]. Moreover, the uniform distribution and minimized aggregation in the composites maximized the reactive sites which could be favorable for photocatalytic reaction[57]. Unlike the ZnO and g-C_3N_4, an obvious increase in roughness was noticed in the hybrids which could be ascribed to the uniform particle assembly on

the surface during heating treatment[56]. Additionally, by the composite formation, the average particle size was greatly reduced from 2.82 µm to 384 nm.

The results providing the chemical compositions are demonstrated in Fig. 3. The EDS of pristine ZnO Fig. 3a depicts the existence of Zn and O, which indicates the phase pure formation. Similarly, the purity of prepared g-C_3N_4 was validated by the evident occurrence of C and N in Fig. 3b. Further, Fig. 3c shows the EDS of the optimized composite containing 10 wt.% g-C_3N_4 with ZnO which has provided the maximum degradation of paracetamol (it will be discussed in subsequent sections) and the existence of Zn, O, C and N elements without impurities justified the purity and accuracy of the synthesis procedure.

To determine the catalytic activity of the nanomaterials, S_{BET} is an important parameter to be taken into view. A higher S_{BET} is accountable for enhanced adsorption of molecules and reduced reaction time. Figure 4a. illustrates nitrogen adsorption/desorption isotherms for pure ZnO, g-C_3N_4 and their composites. The isotherms of adsorption were conducted at 77.3 K at 0.01 to 0.95 P/P_0 relative pressure. The findings revealed that all the composites have a similar isotherm classified as classical type V isotherm hysteresis loop in accordance with IUPAC classification[58], indicating that all the surfaces of composites were mesoporous. In the relative pressure region from 0.6 to 0.9 P/P_0 (see inset of Fig. 4a), the hysteresis loop belongs to H3 type[59], implying the presence of parallel plate slit pore structure[60]. The data for S_{BET} of ZnO, g-C_3N_4 and the composites is provided in Table 2. Interestingly, the surface area measurements followed the surface morphology of the composites (see Fig. 2).

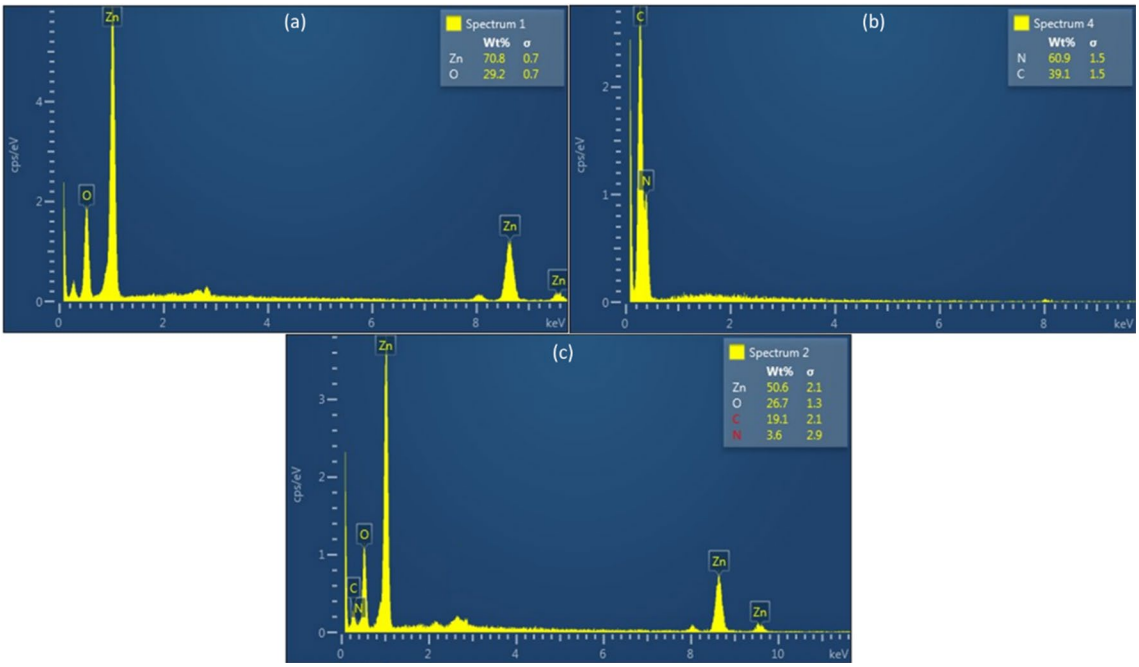

Figure 3. EDS of (**a**) ZnO, (**b**) g-C_3N_4 and (**c**) ZnO/g-$C_3N_4$10% composite.

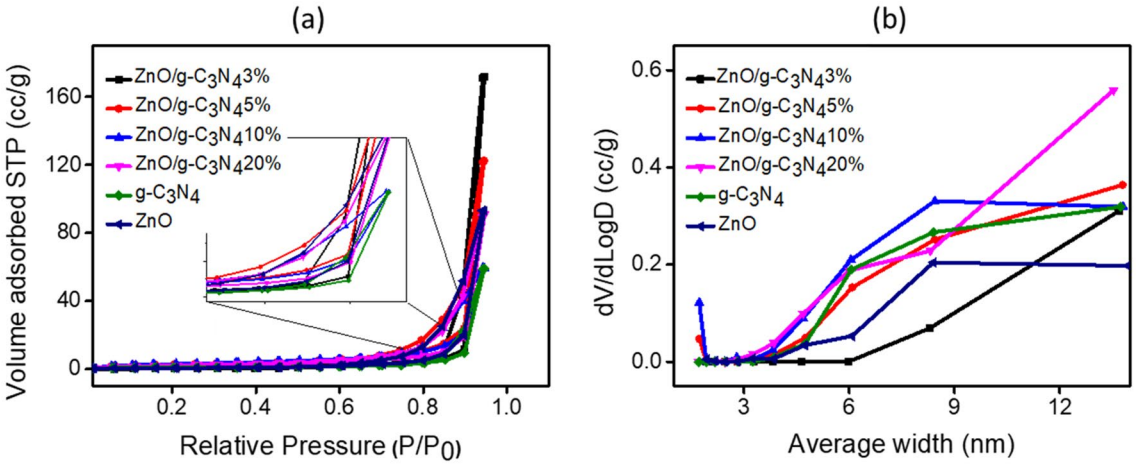

Figure 4. (**a**) Nitrogen adsorption and desorption isotherm with inset an enlarged view of hysteresis loop. (**b**) Pore size distribution of ZnO, g-C_3N_4 and the composites of ZnO/g-C_3N_4.

Catalyst	R^2	Rate constant $\times 10^{-2}$ (min^{-1})	S_{BET} (m^2/g)	Band gap energy (eV)	Degradation (%)
ZnO	–	–	2.335	3.13	4
g-C_3N_4	0.997	2.34	2.728	2.78	75
ZnO/g-$C_3N_4$3%	0.987	2.6	4.091	2.75	78
ZnO/g-$C_3N_4$5%	0.997	3.411	9.935	2.51	87
ZnO/g-$C_3N_4$10%	0.998	5.242	11.335	2.39	95
ZnO/g-$C_3N_4$20%	0.996	2.934	8.137	2.67	82

Table 2. Kinetic rate constant, summary of S_{BET}, band gap energies and relative % degradation by photocatalysts.

As seen from the monographs, the composites look well distributed by raising the g-C_3N_4 loading from 3 to 10 wt.%, this distribution was even more evident at 10 wt.% explaining the increase in the S_{BET} by increasing the wt.% of g-C_3N_4. This factor was related to the high N_2 volume adsorption at higher relative pressure as a result of capillary condensation in mesopores[55]. However, as the loading of g-C_3N_4 increased further to 20 wt.%, the sheets of the g-C_3N_4 looked dominated and covered the ZnO particles (see Fig. 2) revealing a decrease in the S_{BET} which could also be devoted to the blockage of partial g-C_3N_4 nano-sheets[61]. Further, pore size and pore volume distribution was also determined. The average pore diameter ranged between 2 and 4 nm as displayed in Fig. 4b. Improved S_{BET} for the optimized composite could be beneficial for the photocatalytic studies as it is responsible for redox reaction by increasing active sites[62].

The surface chemical composition of the formed ZnO, g-C_3N_4 and ZnO/g-$C_3N_4$10% composite was further examined using XPS (Fig. 5). The C 1s spectrum of g-C_3N_4 was resolved into two component peaks at 284.7 eV and 288.0 eV (Fig. 5a). The one at 284.7 eV was assigned to the aromatic C atom in the carbon nitride matrix (C–C bond) whereas, the other at 288.0 eV was designated to the sp2-bonded carbon attached to the NH_2 group N=C–N[39,63,64]. The N 1s spectrum contained two major peaks along with a lower peak (Fig. 5b), the first at 398.5 eV was attributed to the aromatic nitrogen bonded to two carbon atoms (C=N–C), indicating the appearance of triazine rings[65]. The second shoulder peak at 400.3 eV was linked to the tertiary N atoms ((C–N(–C)–C or C–N(H)–C))[66] while the last peak at 404.2 eV was referred to the charging impacts[67]. The high resolution N1s spectra of synthesized materials (Fig. 5c) showed the increased intensity, indicating the increased content of g-C_3N_4 in composite from 3 to 20 wt%. Provided in the Zn 2p spectrum of ZnO/g-$C_3N_4$10% composite, two major peaks at binding energies of 1045.4 eV and 1022.3 eV were assigned to Zn $2p_{1/2}$ and $2p_{3/2}$ lines respectively (Fig. 5d). The 23.1 eV binding energy separation between these two peaks indicated + 2 states of Zn ions in the composite[39]. However, a shift towards lower binding energy in the composite occurred, indicating the higher

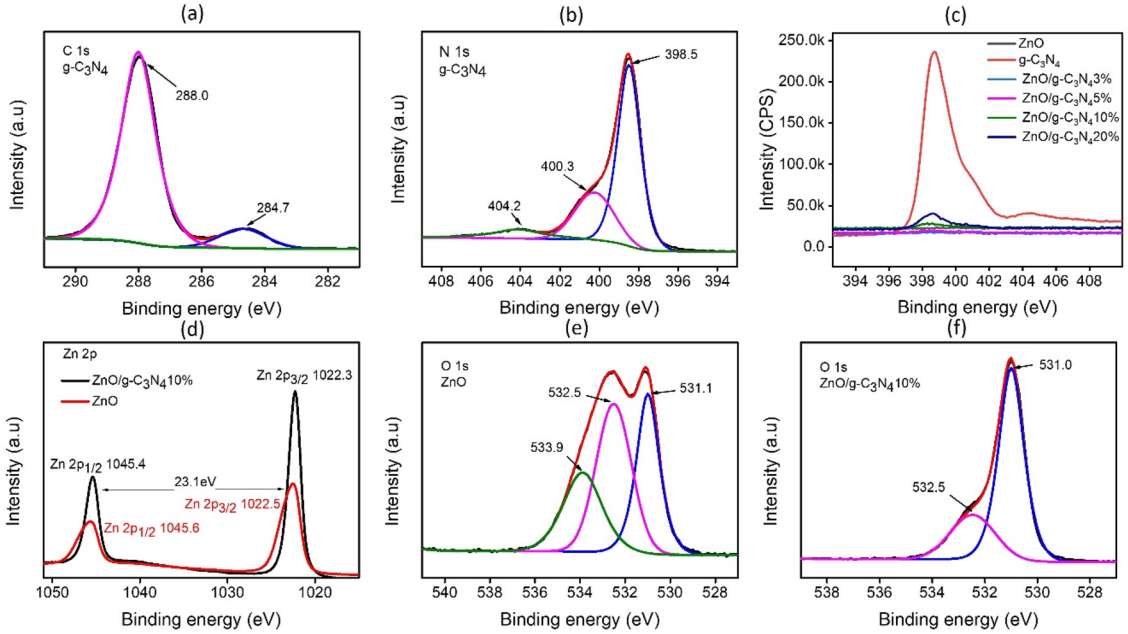

Figure 5. (**a**) high resolution C 1s spectra of g-C_3N_4 (**b**) high resolution N 1s spectra of g-C_3N_4 (**c**) high resolution N 1s spectra of g-C_3N_4, ZnO and ZnO/g-C_3N_4 composites (**d**) high resolution Zn 2p spectra of ZnO/g-$C_3N_4$10% and ZnO (**e**) high resolution O 1s spectra of ZnO (**f**) high resolution O 1s spectra of ZnO/g-$C_3N_4$10%.

electron density in ZnO upon the formation of composite. It means that on contact there is charge transfer from g-C_3N_4 to ZnO[27]. The deconvoluted O 1s line (Fig. 5e) exhibits components at binding energy 531.1 eV, 532.5 eV and 533.9 eV respectively. The first can be linked to the existence of ZnO which is reduced partially such as, ZnO_x, that is in close relation to the presence of O_2^- ions generated by deficiencies of oxygen in the matrix of ZnO[68]. While the second component could be related to physically or chemically adsorbed O_2, OH, and H_2O on the surface[69]. The 533.9 eV peak refers to chemisorbed oxygen or surface hydroxyl bonding of Zn-OH[70]. The 531.0 eV peak in the O 1s spectrum (Fig. 5f) was linked to the participation of O^{2-} particles in zinc and oxygen bonding within the wurtzite ZnO structure[39]. Furthermore, the peak positioned at 532.5 eV could be related to the adsorbed hydroxide group displayed on the surface of composite[39]. In conclusion, the sturdy interfacial bonding encouraged shift of the absorption edge towards the visible region, which could bolster the photocatalytic efficiency by utilizing the maximum spectrum of solar energy[39,66].

Optical properties illustrated in Fig. 6a represent the results obtained by UV–vis DRS spectra. The absorption band of ZnO (wavelength < 400 nm) was observed as earlier reported[71], while the absorption band edge of composites in correlation to g-C_3N_4 and ZnO, experienced a red shift towards higher wavelengths extending between 400 and 460 nm. By the increment in g-C_3N_4 loading, the absorption range of composites was also promoted which resulted in improved utilization of solar light[61]. The band gap energies of g-C_3N_4, ZnO and ZnO/g-C_3N_4 composites were evaluated from Kubelka–Munk (KM) function and determined by slope of the line part to (hν) on the horizontal-axis as displayed in Fig. 6b. From the results shown in Table 2, a decline in band gap with increase in g-C_3N_4 wt.% is evident. Provided a band gap value of 2.39 eV for the optimized composite ZnO/g-$C_3N_4$10%, that match the maximum solar absorption spectrum and hence indicates that the optimized photocatalyst is an efficient candidate to initiate the visible light activated photocatalysis. An effective interaction of g-C_3N_4 and ZnO implied to a well bonded interface among ZnO and g-C_3N_4 phase while forming the composite, hence lowered the band gap energies[51,72]. Thereby, it can provide chances for delayed recombination and extensive transfer of charge carriers[73]. However, a slight increment in the band gap energy on further increasing the g-C_3N_4 loading to 20% could be linked to the quantum size of the active nano particles, electronic interphase impacts and/or smaller interaction between the phases as reported in earlier studies[55].

Photocatalytic study of paracetamol using ZnO/g-C_3N_4 composite

The results obtained by executing UV–Vis spectroscopy measurements ranging from 200 to 400 nm after photodegradation study of paracetamol are shown in Fig. 7a–f. It is evident from the results that unification of ZnO and g-C_3N_4 led to higher degradation of the pharmaceutical under study. It can be observed that paracetamol degradation of only 4% took place by utilizing pure ZnO (Fig. 7a), due to this negligible activity ZnO was not utilized in further experiments. However, the ZnO/g-$C_3N_4$10% as shown in Fig. 7e exhibited enhanced photoactivity and evidently degraded (95%) of the paracetamol in aqueous solution. The amplification in photocatalysis could be because of the separation of charge-carriers, enhanced morphology, lower band gap and higher S_{BET}.

The photocatalytic performance results of fabricated catalysts are demonstrated in Fig. 8a. In 60 min of visible light irradiation, 75% of paracetamol was photocatalytically degraded by pure g-C_3N_4, while 78, 87, 95 and 82% degradation was observed by using ZnO/g-$C_3N_4$3%, ZnO/g-$C_3N_4$5%, ZnO/g-$C_3N_4$10%, and ZnO/g-$C_3N_4$20% respectively under same reaction conditions. Thus, the maximum photodegradation of paracetamol was performed by ZnO/g-$C_3N_4$10% composite. The order of photocatalytic performance was concluded as, ZnO/g-$C_3N_4$10% > ZnO/g-$C_3N_4$5% > ZnO/g-$C_3N_4$20% > ZnO/g-$C_3N_4$3% > g-C_3N_4.

Based on experimental results, a fitting to Eq. (2) was employed for the investigation of kinetic performance of photodegradation and the kinetic plots, ln (C_t/C_0), versus illumination time are exploited in Fig. 8b. From the kinetics outcomes it is obvious that the experimental data is well aligned with pseudo-first-order kinetics and fits well with the kinetic model. Table 2. contains a list of rate-constant (k) along with the correlation-coefficient (R^2). From the data, the highest value of k was determined 5.242×10^{-2} min^{-1} for the ZnO/g-$C_3N_4$10% photocatalyst,

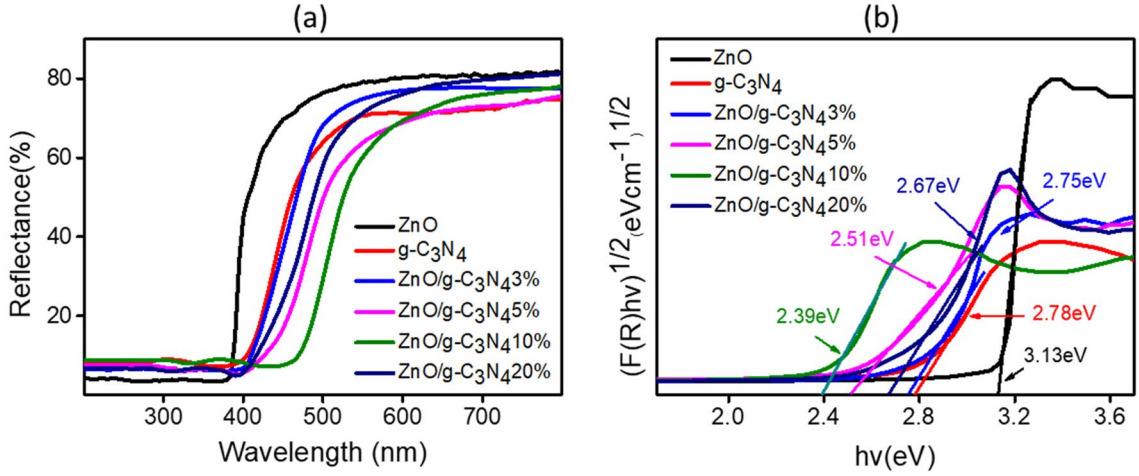

Figure 6. (**a**) UV–Vis diffusive reflection spectra and (**b**) K-M plot of ZnO, g-C_3N_4 and different compositions of ZnO/g-C_3N_4.

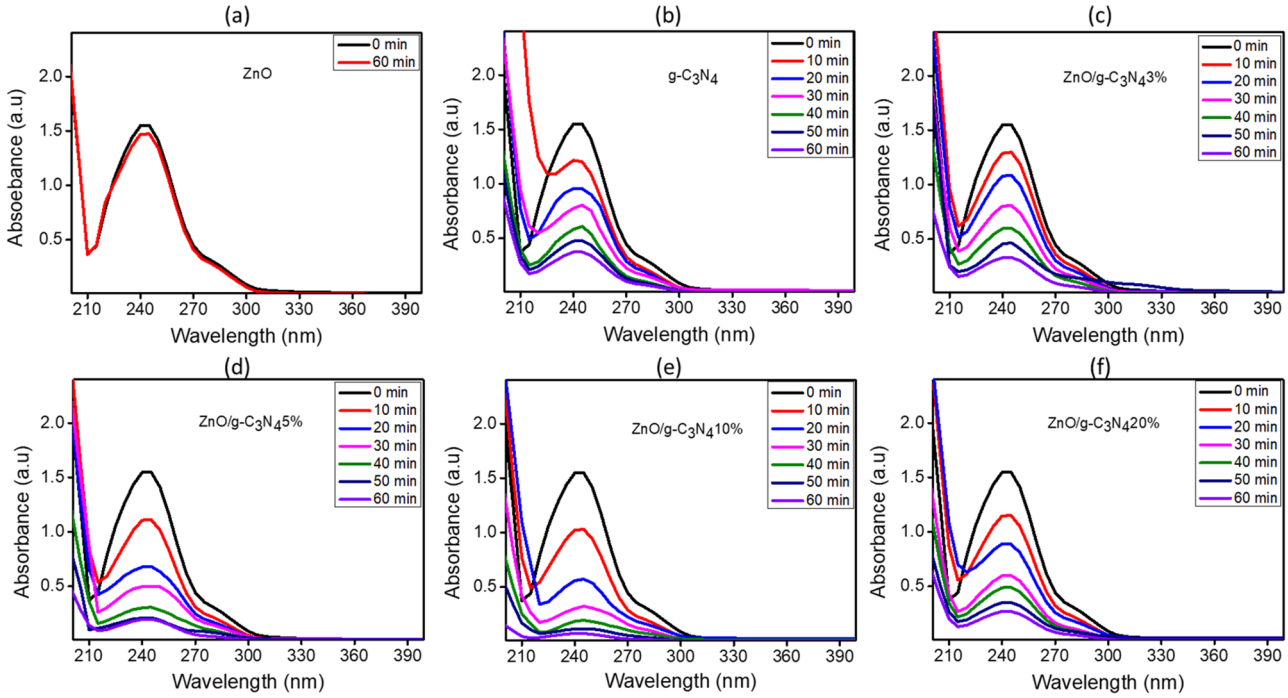

Figure 7. UV–Vis absorption spectra for ZnO, g-C_3N_4 and different compositions of ZnO/g-C_3N_4.

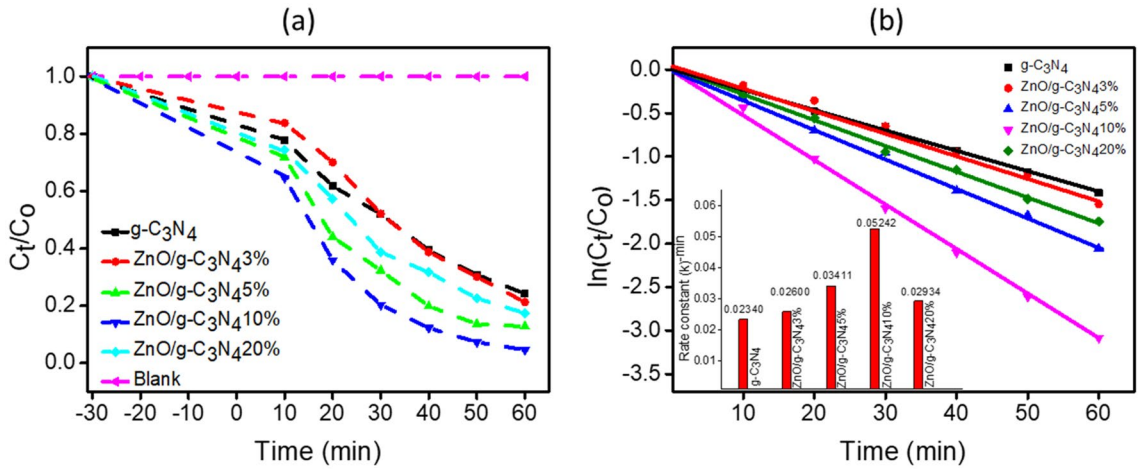

Figure 8. (**a**) Photodegradation of paracetamol versus time (**b**) ln (C_t/C_0) versus time and inset rate constant.

that is much greater compared to pristine g-C_3N_4 (2.340×10^{-2} min^{-1}) for the paracetamol degradation under similar reaction conditions.

In conclusion, by increasing g-C_3N_4 wt.% up to a certain amount, a boost in catalytic performance was observed due to effective charge carrier transportation between g-C_3N_4 to ZnO and suppressed rate of recombination of e^-/ h^+ pair[74]. However, a performance reduction was observed for the composite with more wt.% of g-C_3N_4 than the optimized value due to trapping and poor transfer of electrons followed by increased band gap[53]. After optimizing the suitable photocatalyst i.e., ZnO/g-$C_3N_4$10%, different parameters such as the influence of catalyst amount, drug dosage and pH were also examined.

Effect of parameter on photocatalytic study

The results obtained by monitoring the influence of changing different factors and their impact on the efficiency of photodegradation are depicted in Fig. 9. The impact of photocatalyst quantity in solution and consequent impact on the degradation performance of paracetamol was studied by manipulating the amount of optimized photocatalyst, ZnO/g-$C_3N_4$10%, between 10 and 25 mg in 100 mL drug solution, the outcomes are provided in Fig. 9a. Initially, an increasing trend in degradation efficiency between 80 to 95% was observed by increasing the photocatalyst dose between 10 to 20 mg. However, a drop of efficiency from 95 to 88% was observed by further increasing the catalyst dose amount to 25 mg. For catalyst dosage < 20 mg, the lower photoactivity can be

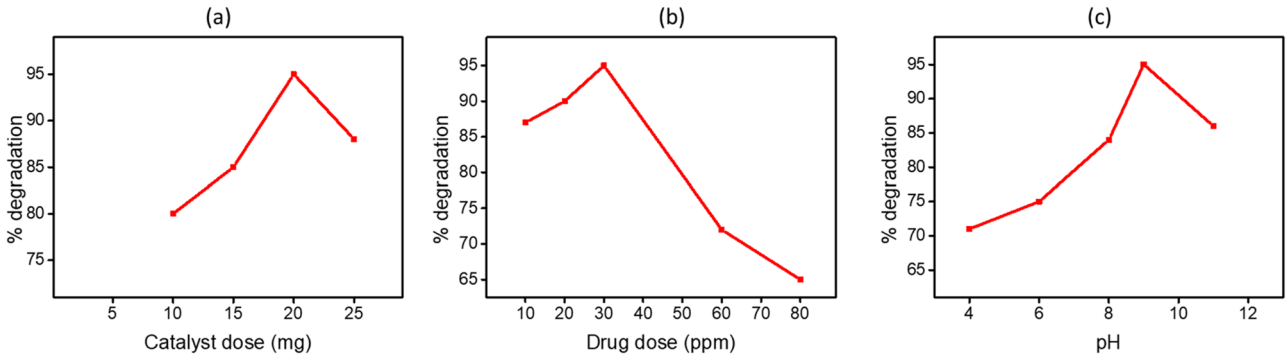

Figure 9. (**a**) Effect of initial catalyst (ZnO/g-$C_3N_4$10%) dose on the photodegradation of paracetamol (**b**) Influence of initial drug dose on the photodegradation of paracetamol using (ZnO/g-$C_3N_4$10%) (**c**) Impact of pH on the photodegradation of paracetamol using (ZnO/g-$C_3N_4$10%).

correlated to the limited number of active-sites for redox reactions. Whereas, the enhancement of photoactivity for dosage 20 mg was attributed to the availability of active sites[75]. However, a drop in effective degradation on furthermore addition of catalyst was credited to the reduced surface area because of the aggregation of catalyst composite resulting in low absorption capacity of photons[49]. Moreover, increased concentration could lead to more scattering of light photons, thereby resulted in poor penetration[53]. Hence, 20 mg dosage of optimized catalyst was selected as the ideal amount for photoactivity.

Another essential parameter in photocatalytic process is the initial drug concentration. To investigate the optimal value of paracetamol concentration, experiments were conducted by changing the paracetamol concentrations between 10 to 80 mg/L and utilizing 20 mg of optimized catalyst. The resultant photodegradation efficiencies were calculated as 87%, 90%, 95%, 72% and 65% for the 10, 20, 30, 60 and 80 mg/L of paracetamol concentration respectively (Fig. 9b). Provided the maximum degradation efficiency, 30 mg/L concentration of paracetamol was selected as an optimal value. At initial pollutant concentration lower than 30 mg/L, the reason for reduced efficiency could be that a trivial quantity of paracetamol was adsorbed on photocatalyst[76]. While, in concentration greater than 30 mg/L, the decrease in efficiency could be reasoned by suppressed path-length and lower penetration of photons[77].

The photocatalytic performance was observed to be highly influenced by varying the solution's pH between 4 and 11 while fixing the photocatalyst dose to 20 mg in 100 mL solution containing 30 mg/L paracetamol. Results provided in Fig. 9c show that at pH 4, 71% paracetamol was degraded followed by 75% degradation on increasing pH value to 6. The increasing trend in degradation efficiency sustained and was increased considerably providing a maximum degradation performance (95%) at pH 9. However, a drop in photodegradation efficiency was observed in stronger alkaline medium at pH 11. At low pH, the consequent lower degradation efficiency could be explained as excessive adsorption of H^+ ions initiated a positive charge on the surface of photocatalyst which caused an electrostatic repulsion to the positive molecules of paracetamol. In comparison, a higher degradation efficiency in alkaline solution of pH 7 and above could be due to a negative charge acquired by the catalyst surface by adsorption of OH^- which then electrostatically attracted the positively charged paracetamol molecules[78]. Moreover, the degradation rate could be triggered by the creation of hydroxyl (•OH) radicals by OH^- in alkaline solution. However, a drop in degradation performance in stronger alkaline solution could be a result of struggle between OH^- and paracetamol molecule to be adsorb on catalyst surface[53].

Reusability test, TOC removal and charge carrier trapping/scavenging analysis

The stability and reusability performance of ZnO/g-$C_3N_4$10% photocatalyst was determined by repetitive four cycles under the same experimental conditions. After each cycle, the photocatalytic composite was recollected and centrifuged at 5000 rpm for 5 min followed by three time washing with distilled water. Before utilizing with a fresh paracetamol solution, the composite obtained after washing was dried in oven at 70 °C till all the water evaporated. As illustrated in Fig. 10a the optimized photocatalyst showed almost consistent photocatalytic efficiency over the four successive cycles. Repetitive runs showed a slight decrement of efficiency (only 3%) between four cycles which revealed the high stability of prepared photocatalyst under visible light illumination and confirmed the reusability several times. Since photocatalyst forms stable suspension with water, there are some chances of losing the sample which could also account for the faint drop in the photoactivity. However, overall study revealed the consistency in percentage degradation of paracetamol in multiple cycles which indicates the promising wide applicability of ZnO/g-$C_3N_4$10% photocatalyst.

To evaluate the extent of mineralization of paracetamol, total organic carbon (TOC) measurement was done for the irradiated solution. Initially the TOC value of stock solution before photocatalysis was 27.4 ppm whereas, after photocatalysis it reduced to 1.88 ppm. Figure 10b shows that 93% of TOC removal was achieved when 95% degradation of paracetamol by ZnO/g-$C_3N_4$10% composite occurred. The findings indicate that the mineralization of paracetamol is consistent with degradation.

The expected reactive species taking part in the photocatalytic study are commonly holes (h^+), hydroxyl and superoxide radical ($O2^{\bullet-}$). To authenticate the capacity of reactive species involved in photocatalysis of paracetamol, charge carrier trapping/scavenging analysis was performed. Isopropanol (IPA) as ($^{\bullet}OH$), ammonium oxalate (AO) as (h^+) and p-benzoquinone (BQ) as ($O2^{\bullet-}$) scavengers were used. Scavengers were added separately before

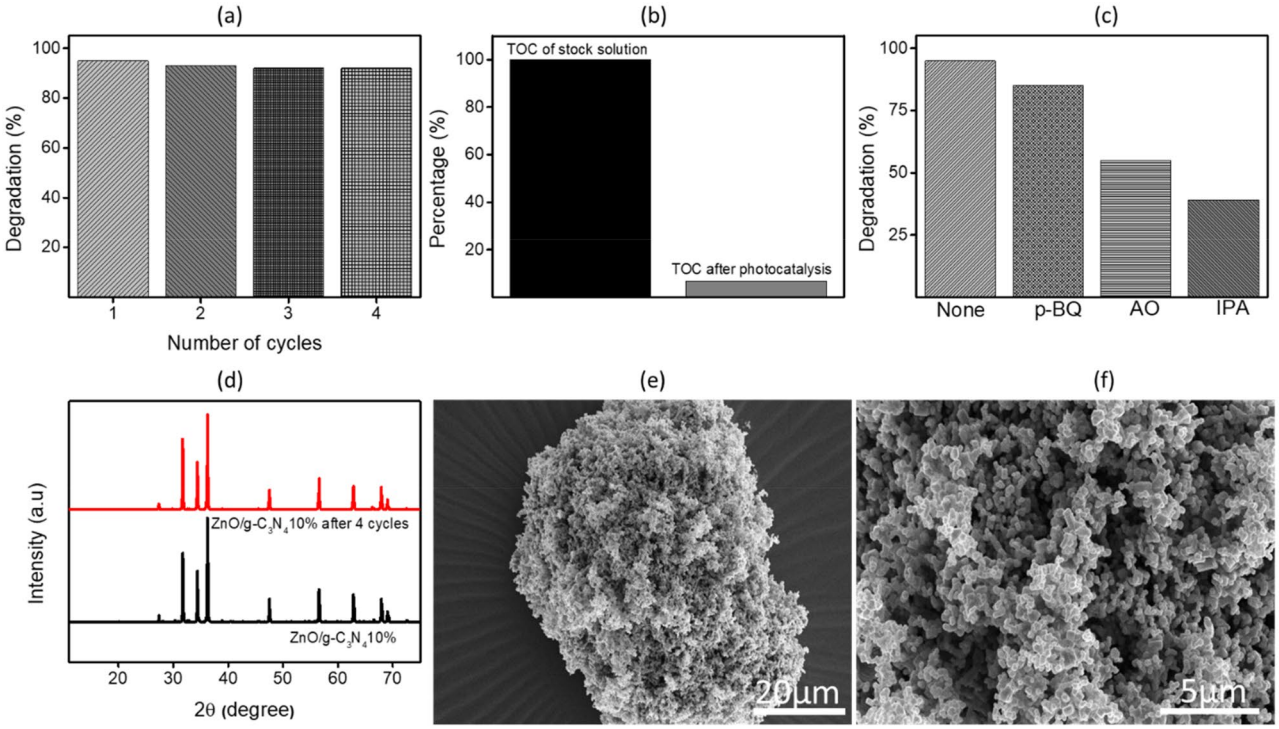

Figure 10. (**a**) Recyclability of ZnO/g-$C_3N_4$10% catalyst in 4-run of cycles (**b**) Percentage of TOC before and after degradation of paracetamol (**c**) charge carrier trapping/scavenging analysis (**d**) XRD of ZnO/g-$C_3N_4$10% before and after 4 cycles (**e**–**f**) FESEM images of ZnO/g-$C_3N_4$10% after 4 cycles.

the start of each experiment with 10 mM concentration in 100 mL. The data presented in Fig. 10c, determines a significant drop in degradation percentage from 95 to 39% upon the addition of IPA which confirms the dominance of (•OH) radicals and their accountability for the photodegradation of paracetamol. To prove the structural stability of photocatalyst, the XRD and FESEM analysis of spent ZnO/g-$C_3N_4$10% was analyzed after four cyclic usages. Figure 10d demonstrates stability by showing no visible change in the XRD pattern of ZnO/g-$C_3N_4$10% photocatalyst before and after the usage. Moreover, FESEM images (Fig. 10e–f) of spent ZnO/g-$C_3N_4$10% clearly depict no change in the morphology compared with surface morphology before usage (see Fig. 2e,e'). Hence, it is confirmed overall stability of ZnO/g-$C_3N_4$10%, suggesting that there is no deterioration of active component during photocatalysis.

Band alignment and photocatalytic degradation mechanisms

To explore the mechanism of charge carrier transport in ZnO/g-$C_3N_4$10% composite, as well as in pure ZnO and pure g-C_3N_4, the ultraviolet photoelectron spectroscopy (UPS) was employed with He I excitation energy ($h\vartheta$ = 21.2 eV), and the outcomes were depicted in Fig. 11a. The analysis of the UPS spectra changes in the composite involved studying the secondary electron energy cutoff (E_{cutOff}) and the valence band maximum (VBM). This was achieved by extrapolating the linear fit to the binding energy cutoff and identifying the intersection point with the UPS spectra baseline[79]. The determined (E_{cutOff}) values were 17.97 eV, 17.67 eV, and 17.21 eV for ZnO, g-C_3N_4, and ZnO/g-$C_3N_4$10%, respectively (shown in Fig. 11b). Additionally, the VBM values were estimated as 2.6 eV, 1.5 eV, and 2.2 eV with respect to ZnO, g-C_3N_4, and the optimized composite (displayed in Fig. 11c). Using the (E_{cutOff}) and VBM values, the energy of the valence band (E_{VB}) and conduction band (E_{CB}) for ZnO, g-C_3N_4, and ZnO/ g-$C_3N_4$10% was calculated through Eqs. (3) and (4)[80,81]. E_{CB} of g-C_3N_4 (− 1.28) was more electronegative than that of ZnO (E_{CB}= − 0.53).

$$E_{VB} = h\vartheta - \left|E_{cutOff} - VBM\right| \tag{3}$$

$$E_{CB} = E_v - E_g \tag{4}$$

The schematic in Fig. 11d depicts the mechanism of charge transfer for photocatalytic degradation by the optimized catalyst which is found to be following S-scheme mechanism[12,26–28]. It can be explained as, before contact (Fig. 11dI), ZnO and g-C_3N_4 have separate band structure and photogenerated electrons could form upon the absorption of energy suitable to band gap. After the contact (Fig. 11dII), electrons would freely transfer from g-C_3N_4 to ZnO, till the fermi lever reaches the equilibrium. At that moment ZnO befits more negative charge, whereas g-C_3N_4 becomes more positive, which created an internal electric field (IE) at the interface. It resulted in band edge bending in both systems. On irradiation (Fig. 11dIII), naturally ZnO and g-C_3N_4 got excited from VB to CB creating the electron hole pair. In the meantime, IE field at the interface and suitable band bending

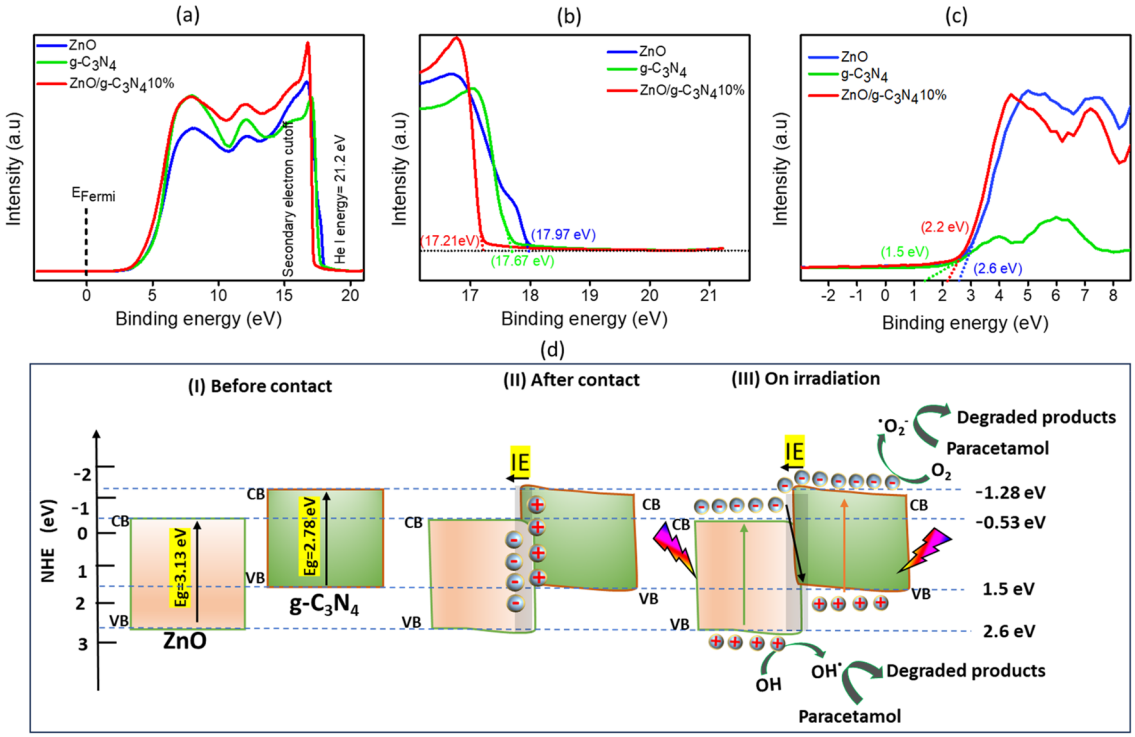

Figure 11. (**a**) UPS spectra, (**b**) He I spectra of secondary electron cutoff, (**c**) valence band maximum spectra of ZnO, g-C_3N_4 and ZnO/g-C_3N_4 (**d**) S-scheme mechanism of photodegradation of paracetamol using ZnO/g-$C_3N_4$10% photocatalyst.

attributed to the recombination of photogenerated electron in ZnO with photogenerated holes in g-C_3N_4 which subsequently facilitated the preservation of photogenerated electron in g-C_3N_4 and photogenerated holes in ZnO. The resulted efficient separation and delayed recombination paid the enhanced redox activity for the optimized composite. The photogenerated electron in CB of g-C_3N_4 reacted with dissolved molecular oxygen forming superoxide anion i.e. $O^{2\bullet-}$ which inducted the paracetamol degradation[50]. In parallel reaction, photo-excited holes on the VB of ZnO interacted with the water molecule and got reduced to form hydroxyl radicals (·OH)[57]. As a result of redox reaction, almost complete photodegradation of paracetamol was achieved. The photocatalytic reactions that occurred are shown in Eqs. (5–8) below.

$$O_2 + CB^{e-} \rightarrow^{\bullet} O_2^- \quad (5)$$

$$^{\bullet}O_2^- + \text{paracetamol} \rightarrow \text{degradation products} \quad (6)$$

$$VB^{h+} + H_2O \rightarrow^{\bullet} OH \quad (7)$$

$$^{\bullet}OH + \text{paracetamol} \rightarrow \text{degradation products} \quad (8)$$

Possible photodegradation pathway

The identification of intermediates generated by the degradation of paracetamol was done by LC-QTOF-MS analysis. The outcomes depicted in Fig. 12a provide evident molecular ion peak at m/z = 152 referred to paracetamol[82]. However, after degradation (Fig. 12b), the hydroxyl radical (•OH) favored the braking of CH_3–C=O in paracetamol molecule to formulate hydroquinone (m/z = 110) which further transformed into cyclohexanol (m/z = 100) by the attack of •OH on the amide group[83]. Phenethyl alcohol (m/z = 122) and another element at m/z = 58 are also among the identified species, moreover, a series of reactions among the formed compounds could produce further more compounds and eventually form water and CO_2[84].

Conclusion

In this study, a practicable and efficient visible light sensitive photocatalytic composite, ZnO/g-C_3N_4, was synthesized successfully by hydrothermal and calcination methods. Four different compositions were formulated by incorporating g-C_3N_4 into ZnO at varying concentrations among which the optimized photocatalyst, ZnO/g-$C_3N_4$10%, exhibited the best activity for the degradation of paracetamol in aqueous solution. The addition of g-C_3N_4 into ZnO matrix has led to a reduction in the band gap from 3.13 to 2.39 eV which resulted in a significant enhancement in light absorption and charge carrier separation. Moreover, a noteworthy increase in the S_{BET} from

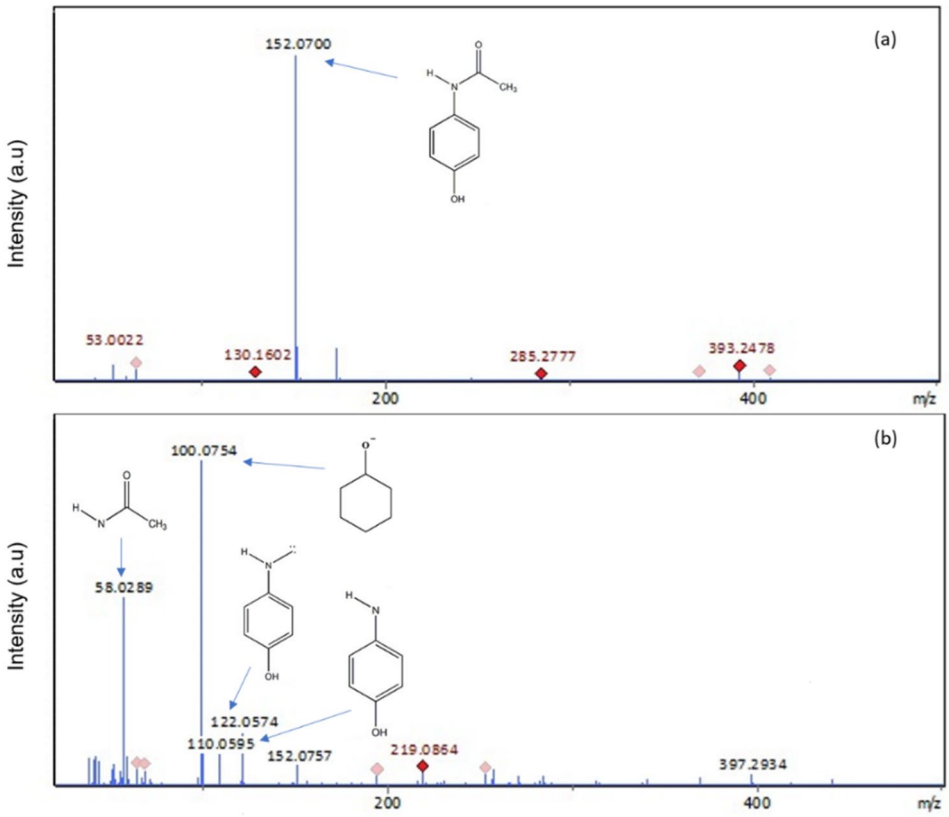

Figure 12. Mass spectra of paracetamol intermediates (**a**) before degradation and (**b**) after degradation with ZnO/g-$C_3N_4$10% composite.

2.33 to 11.33 m^2/g and enhanced morphology provided the grounds for higher activity of the photocatalyst. The study revealed that hydroxyl radicals played a pivotal role in photooxidation and a proposed pathway for degradation was postulated. The intrinsic merits of the synthesized composite such as its ability to actively respond in visible light, straightforward and cost-effective preparation followed by its evident effectiveness makes it a promising catalyst for prospective applications.

Data availability

All data generated or analyzed during this study are included in this published article. All the data are stored on the server of Sharjah University and can be provided upon request from the corresponding author (fahad.hassan@sharjah.ac.ae).

Received: 21 November 2023; Accepted: 21 April 2024
Published online: 28 May 2024

References

1. Moctezuma, E., Leyva, E., Aguilar, C. A., Luna, R. A. & Montalvo, C. Photocatalytic degradation of paracetamol: Intermediates and total reaction mechanism. *J. Hazard. Mater.* **243**, 130–138 (2012).
2. Larsson, D. J. Pollution from drug manufacturing: Review and perspectives. *Philos. Trans. R. Soc. B Biol. Sci.* **369**, 20130571 (2014).
3. Yang, L., Yu, L. E. & Ray, M. B. Photocatalytic oxidation of paracetamol: Dominant reactants, intermediates, and reaction mechanisms. *Environ. Sci. Technol.* **43**, 460–465 (2009).
4. Andreozzi, R., Caprio, V., Marotta, R. & Vogna, D. Paracetamol oxidation from aqueous solutions by means of ozonation and H2O2/UV system. *Water Res.* **37**, 993–1004 (2003).
5. Chaplin, B. P. Critical review of electrochemical advanced oxidation processes for water treatment applications. *Environ. Sci. Process. Impacts* **16**, 1182–1203 (2014).
6. Rizzo, L. *et al.* Degradation of diclofenac by TiO2 photocatalysis: UV absorbance kinetics and process evaluation through a set of toxicity bioassays. *Water Res.* **43**, 979–988 (2009).
7. Hu, J. *et al.* Visible light-enhanced electrocatalytic alcohol oxidation based on two dimensional Pt-BiOBr nanocomposite. *J. Colloid Interface Sci.* **524**, 195–203 (2018).
8. Hoffmann, M. R., Martin, S. T., Choi, W. & Bahnemann, D. W. Environmental applications of semiconductor photocatalysis. *Chem. Rev.* **95**, 69–96 (1995).
9. Dhakshinamoorthy, A. & Garcia, H. Catalysis by metal nanoparticles embedded on metal–organic frameworks. *Chem. Soc. Rev.* **41**, 5262–5284 (2012).
10. Backer, S. N. *et al.* Effect of energy band alignments in carbon doped ZnO/TiO2 hybrid heterojunction photocatalyst on the photodegradation of ofloxacin. *Results Eng.* **20**, 101432 (2023).

11. Xu, Q., Wageh, S., Al-Ghamdi, A. A. & Li, X. Design principle of S-scheme heterojunction photocatalyst. *J. Mater. Sci. Technol.* **124**, 171–173 (2022).
12. Zhu, B., Sun, J., Zhao, Y., Zhang, L. & Yu, J. Construction of 2D S-scheme heterojunction photocatalyst. *Advanced Materials*, 2310600 (2024).
13. Li, Y. *et al.* Comparison of dye photodegradation and its coupling with light-to-electricity conversion over TiO2 and ZnO. *Langmuir* **26**, 591–597 (2010).
14. Dorfman, A., Kumar, N. & Hahm, J.-I. Highly sensitive biomolecular fluorescence detection using nanoscale ZnO platforms. *Langmuir* **22**, 4890–4895 (2006).
15. Wang, J. *et al.* Core-shell g-C3N4@ ZnO composites as photoanodes with double synergistic effects for enhanced visible-light photoelectrocatalytic activities. *Appl. Catal. B Environ.* **217**, 169–180 (2017).
16. Stassi, S. *et al.* Flexible piezoelectric energy nanogenerator based on ZnO nanotubes hosted in a polycarbonate membrane. *Nano Energy* **13**, 474–481 (2015).
17. Guo, Y., Wang, H., He, C., Qiu, L. & Cao, X. Uniform carbon-coated ZnO nanorods: Microwave-assisted preparation, cytotoxicity, and photocatalytic activity. *Langmuir* **25**, 4678–4684 (2009).
18. Zhang, Y. *et al.* The role of Ce doping in enhancing sensing performance of ZnO-based gas sensor by adjusting the proportion of oxygen species. *Sensors Actuators B Chem.* **273**, 991–998 (2018).
19. Vaiano, V., Iervolino, G. & Rizzo, L. Cu-doped ZnO as efficient photocatalyst for the oxidation of arsenite to arsenate under visible light. *Appl. Catal. B Environ.* **238**, 471–479 (2018).
20. Wei, C. *et al.* Nitrogen-doped ZnO/Carbon hollow rhombic dodecahedral for photoelectrochemical sensing glutathione. *Appl. Surf. Sci.* **458**, 872–879 (2018).
21. Liang, X. *et al.* Improved H2 production by ethanol steam reforming over Sc2O3-doped Co-ZnO catalysts. *Catalysts* **7**, 241 (2017).
22. Han, G. *et al.* Enhanced photocatalytic H2O2 production over inverse opal ZnO@ polydopamine S-scheme heterojunctions. *Acta Phys. Chim. Sin.* **38**, 2112037 (2022).
23. Warshagha, Z. A. & Muneer, M. Synthesis of ZnO Co-doped Ph-g-C3N4 for enhanced photocatalytic organic pollutants removal under visible light. *Int. J. Environ. Anal. Chem.* **102**, 6339–6358 (2022).
24. Zheng, L. *et al.* Network structured SnO2/ZnO heterojunction nanocatalyst with high photocatalytic activity. *Inorg. Chem.* **48**, 1819–1825 (2009).
25. Wang, L. *et al.* In-situ growth of g-C3N4 layer on ZnO nanoparticles with enhanced photocatalytic performances under visible light irradiation. *Mater. Lett.* **188**, 347–350 (2017).
26. Jiang, Z., Cheng, B., Zhang, L., Zhang, Z. & Bie, C. A review on ZnO-based S-scheme heterojunction photocatalysts. *Chin. J. Catal.* **52**, 32–49 (2023).
27. Liu, B. *et al.* Hierarchically porous ZnO/g-C3N4 S-scheme heterojunction photocatalyst for efficient H2O2 production. *Langmuir* **37**, 14114–14124 (2021).
28. Sayed, M. *et al.* EPR investigation on electron transfer of 2D/3D g-C3N4/ZnO S-scheme heterojunction for enhanced CO2 photoreduction. *Adv. Sustain. Syst.* **6**, 2100264 (2022).
29. Zhao, Z., Sun, Y. & Dong, F. Graphitic carbon nitride based nanocomposites: A review. *Nanoscale* **7**, 15–37 (2015).
30. Shi, F. *et al.* ZnS microsphere/gC 3 N 4 nanocomposite photo-catalyst with greatly enhanced visible light performance for hydrogen evolution: synthesis and synergistic mechanism study. *RSC Adv.* **4**, 62223–62229 (2014).
31. Hao, X., Ji, X. & Zhang, Q. Effective improvement of the photocatalytic efficiency of g-C3N4 by a green hydrothermal treatment method. *Mater. Lett.* **185**, 29–31 (2016).
32. Su, F. *et al.* mpg-C3N4-catalyzed selective oxidation of alcohols using O2 and visible light. *J. Am. Chem. Soc.* **132**, 16299–16301 (2010).
33. Hu, S. *et al.* Facile synthesis of Fe3O4/g-C3N4/HKUST-1 composites as a novel biosensor platform for ochratoxin A. *Biosensors Bioelectron.* **92**, 718–723 (2017).
34. Pang, X. *et al.* A bio-chemical application of N-GQDs and g-C3N4 QDs sensitized TiO2 nanopillars for the quantitative detection of pcDNA3-HBV. *Biosensors Bioelectron.* **91**, 456–464 (2017).
35. Zhao, Y., Shalom, M. & Antonietti, M. Visible light-driven graphitic carbon nitride (g-C3N4) photocatalyzed ketalization reaction in methanol with methylviologen as efficient electron mediator. *Appl. Catal. B Environ.* **207**, 311–315 (2017).
36. Yuan, X. *et al.* Enhanced catalytic ozonation performance of highly stabilized mesoporous ZnO doped g-C3N4 composite for efficient water decontamination. *Appl. Catal. A General* **551**, 129–138 (2018).
37. Wang, Y., Shi, R., Lin, J. & Zhu, Y. Enhancement of photocurrent and photocatalytic activity of ZnO hybridized with graphite-like C 3 N 4. *Energy Environ. Sci.* **4**, 2922–2929 (2011).
38. Jin, C. *et al.* Efficient photocatalytic degradation and adsorption of tetracycline over type-II heterojunctions consisting of ZnO nanorods and K-doped exfoliated g-C3N4 nanosheets. *Ind. Eng. Chem. Res.* **59**, 2860–2873 (2020).
39. Zhu, Y.-P., Li, M., Liu, Y.-L., Ren, T.-Z. & Yuan, Z.-Y. Carbon-doped ZnO hybridized homogeneously with graphitic carbon nitride nanocomposites for photocatalysis. *J. Phys. Chem. C* **118**, 10963–10971 (2014).
40. Park, T. J., Pawar, R. C., Kang, S. & Lee, C. S. Ultra-thin coating of gC 3 N 4 on an aligned ZnO nanorod film for rapid charge separation and improved photodegradation performance. *RSC Adv.* **6**, 89944–89952 (2016).
41. Gao, Z. *et al.* Aminated flower-like ZnIn2S4 coupled with benzoic acid modified g-C3N4 nanosheets via covalent bonds for ameliorated photocatalytic hydrogen generation. *Appl. Catal. B Environ.* **268**, 118462 (2020).
42. Zhang, J. *et al.* Co-monomer control of carbon nitride semiconductors to optimize hydrogen evolution with visible light. *Angew. Chem. Int. Edn.* **51**, 3183–3187 (2012).
43. Lian, X. *et al.* Construction of S-scheme Bi2WO6/g-C3N4 heterostructure nanosheets with enhanced visible-light photocatalytic degradation for ammonium dinitramide. *J. Hazard. Mater.* **412**, 125217 (2021).
44. Li, K. *et al.* Synthesis of g-C3N4 derived from different precursors for photodegradation of sulfamethazine under visible light. *Processes* **11**, 528 (2023).
45. Li, T., Cai, H., Li, C., Liu, X. & Huang, F. Rocksalt-Zincblende–Wurtzite mixed-phase ZnO crystals with high activity as photocatalysts for visible-light-driven water splitting. *Front. Chem.* **8**, 351 (2020).
46. Liu, Y. *et al.* Phenanthroline bridging graphitic carbon nitride framework and Fe (II) ions to promote transfer of photogenerated electrons for selective photocatalytic reduction of Nitrophenols. *J. Colloid Interface Sci.* **608**, 2088–2099 (2022).
47. Lin, C. *et al.* Photocatalytic oxidation removal of fluoride ion in wastewater by gC 3 N 4/TiO 2 under simulated visible light. *Adv. Compos. Hybrid Mater.* **4**, 339–349 (2021).
48. He, Y., Zhang, L., Teng, B. & Fan, M. New application of Z-scheme Ag3PO4/g-C3N4 composite in converting CO2 to fuel. *Environ. Sci. Technol.* **49**, 649–656 (2015).
49. Girish, Y. R. *et al.* Rapid and facile synthesis of Z-scheme ZnO/g-C3N4 heterostructure as efficient visible light-driven photocatalysts for dye degradation and hydrogen evolution reaction. *J. Hazardous Mater. Adv.* **9**, 100230 (2023).
50. Kumar, S., Tonda, S., Baruah, A., Kumar, B. & Shanker, V. Synthesis of novel and stable gC 3 N 4/N-doped SrTiO 3 hybrid nanocomposites with improved photocurrent and photocatalytic activity under visible light irradiation. *Dalton Trans.* **43**, 16105–16114 (2014).
51. Sun, J.-X. *et al.* Fabrication of composite photocatalyst gC 3 N 4–ZnO and enhancement of photocatalytic activity under visible light. *Dalton Trans.* **41**, 6756–6763 (2012).

52. Md Rosli, N. I., Lam, S.-M., Sin, J.-C., Satoshi, I. & Mohamed, A. R. Photocatalytic performance of ZnO/g-C 3 N 4 for removal of phenol under simulated sunlight irradiation. *J. Environ. Eng.* **144**, 04017091 (2018).
53. Meena, P. L., Poswal, K., Surela, A. K. & Saini, J. K. Fabrication of g-C3N4/ZnO Nanoheterostructures for Effective Degradation of Methylene Blue Dye under Visible Light Irradiation. (2022).
54. Swamy, C. K. *et al.* Microwave hydrothermal synthesis of copper induced ZnO/gC3N4 heterostructure with efficient photocatalytic degradation through S-scheme mechanism. *J. Photochem. Photobiol. A Chem.* **418**, 113394 (2021).
55. Pérez-Molina, Á., Pastrana-Martínez, L. M., Pérez-Poyatos, L. T., Morales-Torres, S. & Maldonado-Hódar, F. J. One-pot thermal synthesis of g-C3N4/ZnO composites for the degradation of 5-fluoruracil cytostatic drug under UV-LED irradiation. *Nanomaterials* **12**, 340 (2022).
56. Kong, J.-Z. *et al.* Visible light-driven photocatalytic performance of N-doped ZnO/gC 3 N 4 nanocomposites. *Nanoscale Res. Lett.* **12**, 1–10 (2017).
57. Huo, P. *et al.* Incorporation of N-ZnO/CdS/Graphene oxide composite photocatalyst for enhanced photocatalytic activity under visible light. *J. Alloys Compds.* **670**, 198–209 (2016).
58. Sing, K. S. Reporting physisorption data for gas/solid systems with special reference to the determination of surface area and porosity (Recommendations 1984). *Pure Appl. Chem.* **57**, 603–619 (1985).
59. Yurdakal, S., Garlisi, C., Özcan, L., Bellardita, M. & Palmisano, G. *Heterogeneous photocatalysis* 87–152 (Elsevier, 2019).
60. Zhang, Y. *et al.* The pore size distribution and its relationship with shale gas capacity in organic-rich mudstone of Wufeng-Longmaxi Formations, Sichuan Basin, China. *J. Natl. Gas Geosci.* **1**, 213–220 (2016).
61. Zhang, B. *et al.* Pompon-like structured gC 3 N 4/ZnO composites and their application in visible light photocatalysis. *Res. Chem. Intermediates* **44**, 6895–6906 (2018).
62. Mohtar, S. S. *et al.* Impact of doping and additive applications on photocatalyst textural properties in removing organic pollutants: A review. *Catalysts* **11**, 1160 (2021).
63. She, X. *et al.* Template-free synthesis of 2D porous ultrathin nonmetal-doped g-C3N4 nanosheets with highly efficient photocatalytic H2 evolution from water under visible light. *Appl. Catal. B Environ.* **187**, 144–153 (2016).
64. Yao, C. *et al.* Facile surface modification of textiles with photocatalytic carbon nitride nanosheets and the excellent performance for self-cleaning and degradation of gaseous formaldehyde. *J. Colloid Interface Sci.* **533**, 144–153 (2019).
65. Zhu, B., Xia, P., Ho, W. & Yu, J. Isoelectric point and adsorption activity of porous g-C3N4. *Appl. Surf. Sci.* **344**, 188–195 (2015).
66. Paul, D. R. *et al.* ZnO-modified g-C3N4: A potential photocatalyst for environmental application. *ACS Omega* **5**, 3828–3838 (2020).
67. Oh, W.-D., Lok, L.-W., Veksha, A., Giannis, A. & Lim, T.-T. Enhanced photocatalytic degradation of bisphenol A with Ag-decorated S-doped g-C3N4 under solar irradiation: Performance and mechanistic studies. *Chem. Eng. J.* **333**, 739–749 (2018).
68. Li, L. *et al.* Properties of Al heavy-doped ZnO thin films by RF magnetron sputtering. *Mater. Res. Bull.* **43**, 1456–1462 (2008).
69. Tomić, M. *et al.* Zno structures with surface nanoscale interfaces formed by Au, Fe2O3, or Cu2O modifier nanoparticles: Characterization and gas sensing properties. *Sensors* **21**, 4509 (2021).
70. Zhang, X. *et al.* Effect of aspect ratio and surface defects on the photocatalytic activity of ZnO nanorods. *Sci. Rep.* **4**, 4596 (2014).
71. Mirikaram, N. *et al.* Photocatalytic perfomance of ZnO-graphene oxide composites towards the degradation of vanillic acid under solar radiation and visible-LED. *Nanomaterials* **11**, 1576 (2021).
72. Jo, W.-K. & Selvam, N. C. S. Enhanced visible light-driven photocatalytic performance of ZnO–g-C3N4 coupled with graphene oxide as a novel ternary nanocomposite. *J. Hazardous Mater.* **299**, 462–470 (2015).
73. Wu, M. *et al.* Template-free synthesis of nanocage-like gC 3 N 4 with high surface area and nitrogen defects for enhanced photocatalytic H 2 activity. *J. Mater. Chem. A* **7**, 5324–5332 (2019).
74. Kalisamy, P., Lallimathi, M., Suryamathi, M., Palanivel, B. & Venkatachalam, M. ZnO-embedded S-doped gC 3 N 4 heterojunction: Mediator-free Z-scheme mechanism for enhanced charge separation and photocatalytic degradation. *RSC Adv.* **10**, 28365–28375 (2020).
75. Barzgari, Z., Ghazizadeh, A. & Askari, S. Z. Preparation of Mn-doped ZnO nanostructured for photocatalytic degradation of Orange G under solar light. *Res. Chem. Intermediates* **42**, 4303–4315 (2016).
76. Osman, H., Su, Z. & Ma, X. Efficient photocatalytic degradation of Rhodamine B dye using ZnO/graphitic C 3 N 4 nanocomposites synthesized by microwave. *Environ. Chem. Lett.* **15**, 435–441 (2017).
77. Pawar, R. C., Son, Y., Kim, J., Ahn, S. H. & Lee, C. S. Integration of ZnO with g-C3N4 structures in core–shell approach via sintering process for rapid detoxification of water under visible irradiation. *Curr. Appl. Phys.* **16**, 101–108 (2016).
78. Tseng, I.-H., Sung, Y.-M., Chang, P.-Y. & Chen, C.-Y. Anatase TiO2-decorated graphitic carbon nitride for photocatalytic conversion of carbon dioxide. *Polymers* **11**, 146 (2019).
79. Choi, J. Y. *et al.* Effect of Si on the energy band gap modulation and performance of silicon indium zinc oxide thin-film transistors. *Sci. Rep.* **7**, 15392 (2017).
80. Wang, G. *et al.* Aqueous phase synthesis and enhanced field emission properties of ZnO-sulfide heterojunction nanowires. *Sci. Rep.* **6**, 29470 (2016).
81. Suyana, P. *et al.* Co 3 O 4–C 3 N 4 p–n nano-heterojunctions for the simultaneous degradation of a mixture of pollutants under solar irradiation. *Environ. Sci. Nano* **4**, 212–221 (2017).
82. Dalmázio, I., Alves, T. & Augusti, R. An appraisal on the degradation of paracetamol by TiO2/UV system in aqueous medium: Product identification by gas chromatography-mass spectrometry (GC-MS). *J. Braz. Chem. Soc.* **19**, 81–88 (2008).
83. Zia, J. & Riaz, U. Microwave-assisted degradation of paracetamol drug using polythiophene-sensitized Ag–Ag2O heterogeneous photocatalyst derived from plant extract. *ACS Omega* **5**, 16386–16394 (2020).
84. Guerra, M. H. *et al.* Oxidation mechanisms of amoxicillin and paracetamol in the photo-Fenton solar process. *Water Res.* **156**, 232–240 (2019).

Acknowledgements

The work was supported by the University of Sharjah Grant Number UoS-130508, PI: Abdallah Shanableh. The authors are very grateful to acknowledge the Research Institute of Sciences & Engineering, the Advanced Materials Research Laboratory, and the Environmental Analytical Laboratory staff at the University of Sharjah.

Author contributions

F. H contributed to the conceptualization, methodology, validation, formal analysis, investigation, data curation, and writing the original draft. He also participated in the review and editing process. S. N B.'s contributions include proofreading, technique analysis, and visualization. I. W A. engaged in proofreading provided resources, and contributed to the review and editing process. M. A. took on roles in supervision, and visualization, and participated in the review and editing process. He also contributed to conceptualization. A.S. played a key role in supervision, fund acquisition, conceptualization, resourcing, and investigation. M. E. contributed strongly to supervision, conceptualization, and scientific investigation. review editing and proofreading.

Competing interests
The authors declare no competing interests.

Additional information
Correspondence and requests for materials should be addressed to F.H., M.E. or A.S.

Reprints and permissions information is available at www.nature.com/reprints.

Publisher's note Springer Nature remains neutral with regard to jurisdictional claims in published maps and institutional affiliations.